Supplementary Information for:

Scannable dual-focus metalens with hybrid phase

Gi-Hyun Go, Chung Hyun Park, Kie Young Woo, Minho Choi & Yong-Hoon Cho*

Department of Physics and KI for the NanoCentury, Korea Advanced Institute of Science and Technology (KAIST), Daejeon 34141, Republic of Korea.

Corresponding authors: * yhc@kaist.ac.kr

Supplementary Text

In the main text, we have reported a scannable dual-focus metalens using a hybrid phase. In this supplementary information, we present the details of the experimental methods, results, and corresponding numerical calculations.

Supplementary Note 1: Design of a hybrid phase profile

To understand the aberrations of single-layer metalens, we investigate the ray traces of hyperbolic and quadratic phases. The hyperbolic phase profile can be described as

$$\phi_H(x,y) = -\frac{2\pi}{\lambda}\left(\sqrt{x^2+y^2+f^2}-f\right), \quad (1)$$

with f the focal length. While perfect focusing is generated at the focal plane for a planar wavefront at normal incidence, a hyperbolic phase profile is not optimized for obliquely incident beams. The desired phase profile that creates a focal spot at $(ftan\theta, 0, f)$ for an obliquely incident beam in the x-direction becomes

$$\phi(x,y) = -\frac{2\pi}{\lambda}\left(\sqrt{f^2+(x-ftan\theta)^2+y^2}+x\sin\theta\right), \quad (2)$$

where θ denotes the angle of incidence. The phase $\phi(x,y)$ in Equation (2) approximates $\phi_H(x,y)$ in Equation (1) for a low numerical aperture (NA). For high-NA metalenses, however, the approximation does not work, inducing off-axis aberrations, which severely limit the scan range (SR).

A quadratic phase profile was proposed and developed for single-layer wide SR metalens. The quadratic phase profile is described as

$$\phi_Q(x,y) = -\frac{\pi}{f\lambda}(x^2+y^2). \quad (3)$$

In this phase, the effect of oblique incidence is a spatial translation of the focal spot as follows:

$$\phi(x,y) = -\frac{\pi}{f\lambda}(x^2+y^2)+\frac{2\pi}{\lambda}xsin\theta = -\frac{\pi}{f\lambda}((x-fsin\theta)^2+y^2)+\frac{f}{2}sin^2\theta. \quad (4)$$

A linear phase, which is imposed by a plane wave at oblique incidence, results in spatial translation of the focal spot. Therefore, the quadratic phase achieves a wide SR. However, the quadratic phase introduces spherical aberrations and reduces NA.

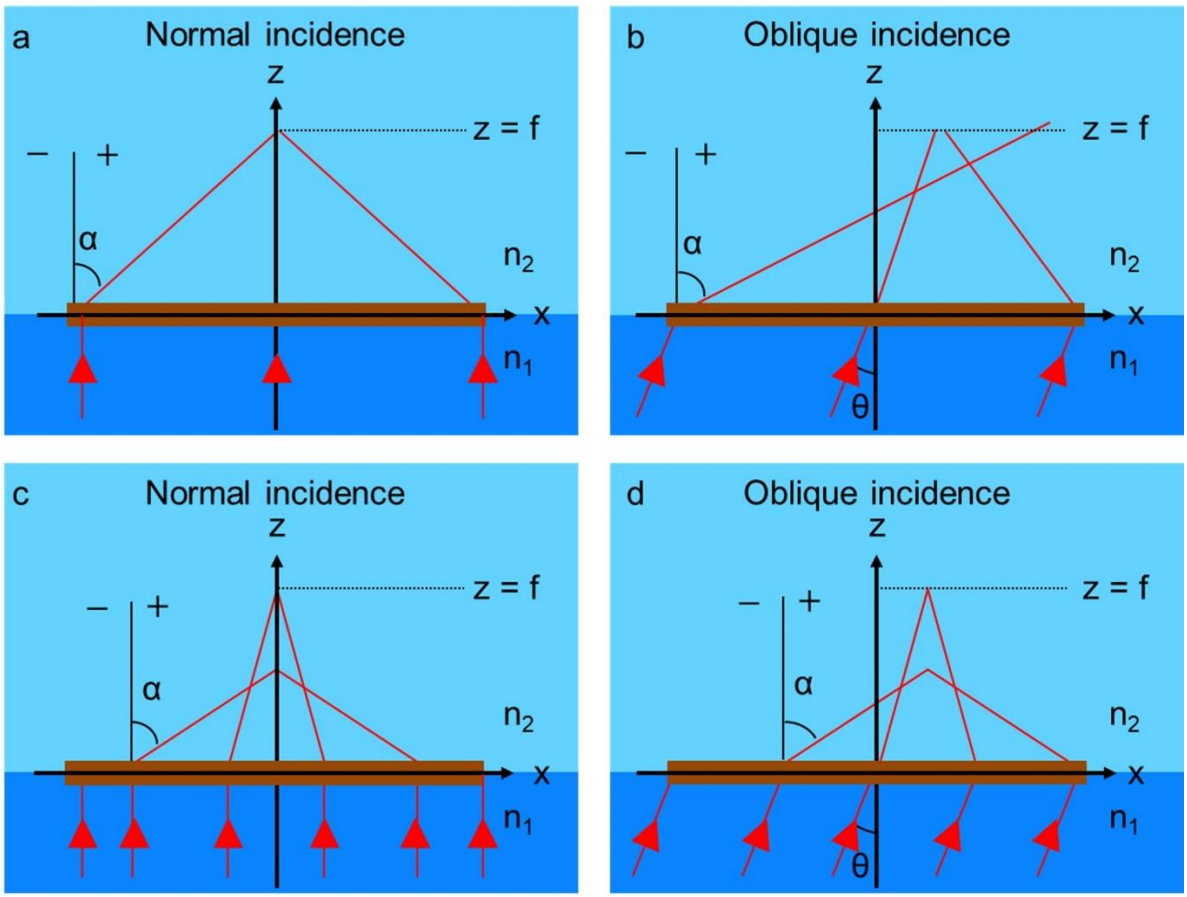

Supplementary Figure 1. a Hyperbolic phase profile for normal incidence. **b** Hyperbolic phase profile for oblique incidence. **c** Quadratic phase profile for normal incidence. **d** Quadratic phase profile for oblique incidence.

We investigate each aberration using the generalized Snell's law.

$$sin\alpha = \frac{1}{k}\frac{\partial \phi}{\partial x}, \tag{5}$$

where k denotes the wave vector in the propagation area. Supplementary Figure 1a and 1b show the bending of the light entering the hyperbolic metalens. In the case of normal incidence, the chief ray passing through the centre and the marginal ray passing through the edge meet at exactly one point. However, in the case of oblique incidence, the marginal ray on the left edge is sharply bent, and thus the chief ray and marginal ray do not meet at a point, resulting in an off-axis aberration. In the case of the quadratic phase profile (Supplementary Figure 1c and 1d), spherical aberration occurs because the chief ray of the centre and the marginal ray of the edge do not meet at the same point for the normal incident beam introducing an effective aperture. Phase modulation outside the effective aperture is so rapid that the diffracted rays become evanescent. For oblique incidence, the position of the effective aperture moves as the light tilts, and the marginal ray that causes the off-axis aberration does not influence the focus.

Inspired by previous results, we consider a hybrid phase consisting of hyperbolic and quadratic phases. The hyperbolic phase inside reduces the spherical aberration, and the quadratic phase outside reduces the off-axis aberrations. This hybrid phase profile with boundary $r = r_0$ is described as follows:

for $r < r_0$,

$$\phi_{Hyb}(r) = -\frac{2\pi n_w}{\lambda}\left(\sqrt{f^2 + r^2} - f\right) \quad (6)$$

for $r > r_0$,

$$\phi_{Hyb}(r) = -\frac{\pi n_w}{\lambda\sqrt{f^2 + r_0^2}}(r^2 - r_0^2) + \phi_{Hyb}(r_0), \quad (7)$$

where n_w, λ, f, and r are the refractive index of water, wavelength, focal length and radial coordinate, respectively.

Supplementary Note 2: Geometry of the metalens

High-NA lenses with an NA above 1 can only be achieved via immersion in high-index liquids. There are two types of immersion metalenses, as shown in Supplementary Figure 2. We selected the front-immersion geometry because the front-immersion metalens does not constrain the working distance. The refractive index of silicon is sufficiently high to realize a front-immersion metalens.

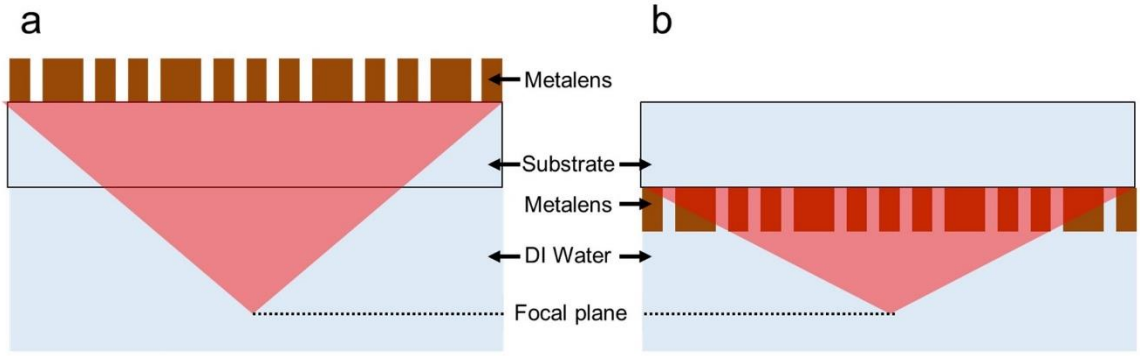

Supplementary Figure 2. Immersion geometry of a metalens. a Back-immersion geometry. **b** Front-immersion geometry.

Supplementary Note 3: Ray traces

We compared the ray traces for the hyperbolic, quadratic, and hybrid phases with the boundary r_0 = 18 μm, as shown in Supplementary Figure 3. Each metalens was located at z = 0. The size and focal length of all the metalenses were 170.6 μm and 20 μm, respectively. The results from Supplementary Note 1 are even more apparent in the ray traces. The rays for a metalens with a hyperbolic phase profile perfectly meet at one point under normal incidence. However, in the case of oblique incidence, the marginal ray on the left edge is sharply bent, and thus the chief ray and marginal ray do not meet at a point, resulting in an off-axis aberration. Note that rays on the left edge cause off-axis aberrations. In the quadratic phase profile, the phase modulation is so rapid that diffracted rays outside the effective aperture become evanescent. An effective aperture has two conflicting perspectives. The effective aperture not only reduces off-axis aberration but also hinder the delivery of high-k components for an NA of 0.9 or higher. The ray traces of the hybrid phase are shown in Supplementary Figure 3c. The ray traces of the hybrid phase and the quadratic phase profile are virtually unchanged for incident angles as high as 2°, which are much more tolerant than ray traces of the hyperbolic phase. Note that the aperture size of the hybrid phase is larger than that of the quadratic phase for delivering the high-k components.

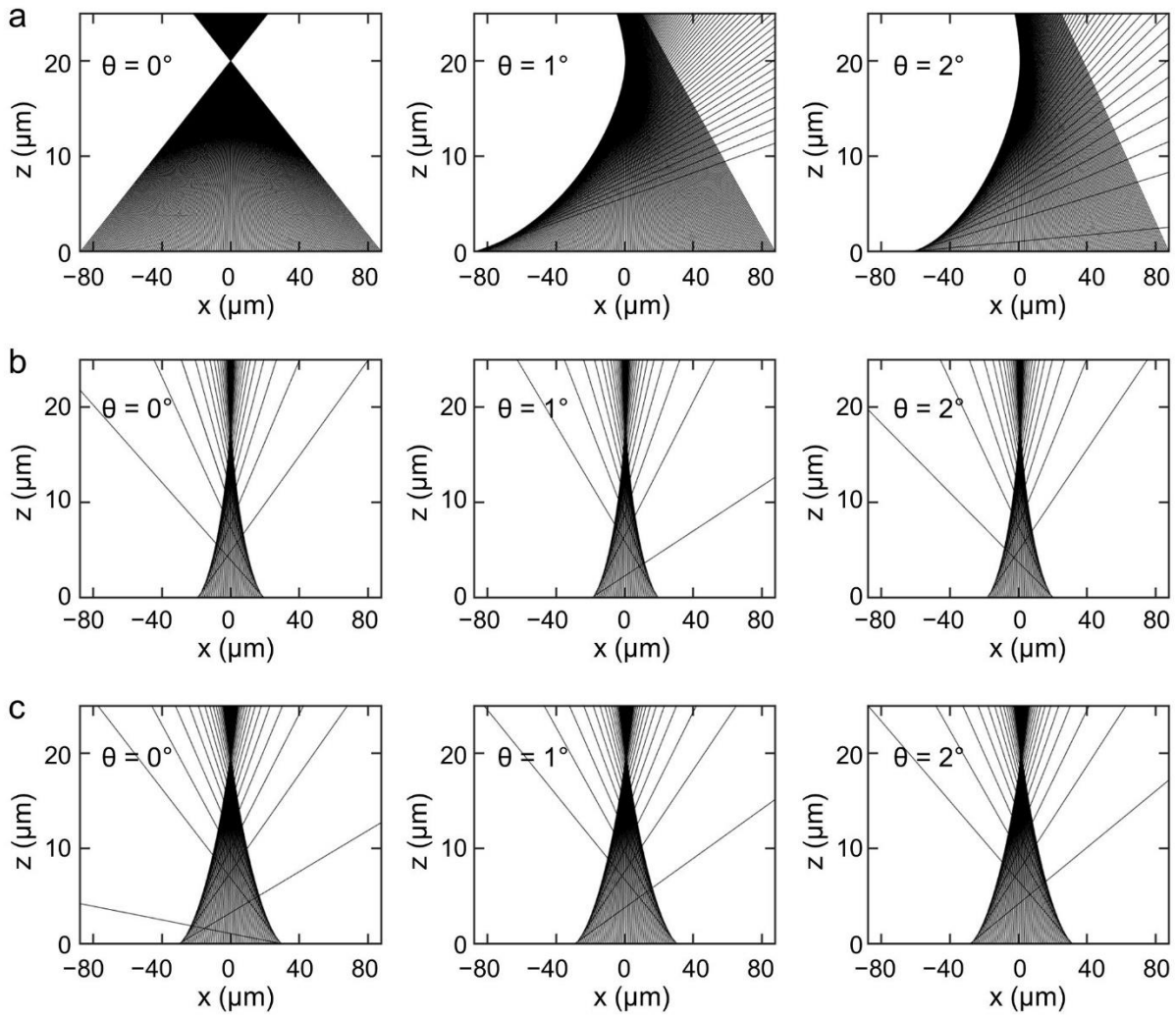

Supplementary Figure 3. Ray traces results. a Hyperbolic phase profile. **b** Quadratic phase profile. **c** Hybrid phase profile.

Supplementary Note 4: NA and displacement with varying r_0

In the main text, we calculated the focal spots for each metalens using the Kirchhoff diffraction integral, a physically rigorous form of the Huygens-Fresnel principle. The NA and lateral displacement of the focal spot are obtained from the calculated focal spots. Supplementary Figure 4 shows the NA and displacement of the focal spot for the hybrid phase with varying boundaries. We found two interesting aspects of a hybrid phase with different boundaries. First, the balance between NA and SR can be easily controlled by changing the boundary (Supplementary Figure 4a). Second, the displacements of the calculated focal spots depend on the boundary (Supplementary Figure 4b). This result can be interpreted as a hybrid phase outside the boundary, as described in Equation (6). For oblique incidence, Equation (6) becomes

for $r > r_0$,

$$\phi_{Hyb}(r > r_0) = -\frac{\pi n_w}{\lambda\sqrt{f^2 + r_0^2}}(r^2 - r_0^2) + \phi_H(r_0) + \frac{2\pi n_s}{\lambda} x \sin\theta$$
$$= -\frac{\pi n_w}{\lambda\sqrt{f^2 + r_0^2}}\left\{\left(x - \frac{n_s}{n_w}\sqrt{f^2 + r_0^2}\, sin\,\theta\right)^2 + y^2\right\} + \frac{\pi n_s^2}{\lambda n_w}\frac{\sqrt{f^2 + r_0^2}}{2} sin^2\theta \quad (8)$$

where n_s is the refractive index of the sapphire substrate. The effect of oblique incidence is the spatial translation of the focal spot, and the displacement is proportional $\sqrt{f^2 + r_0^2}\, sin\,\theta$. Therefore, it had a wider scanning range than the quadratic phase for the same incident angle. Here, we confirm that metalenses with a hybrid phase profile and a diameter of 160 μm have a scan range of 2.5 μm × 2.5 μm with high NA>0.9. The scan range can increase as the size of the metalens increases.

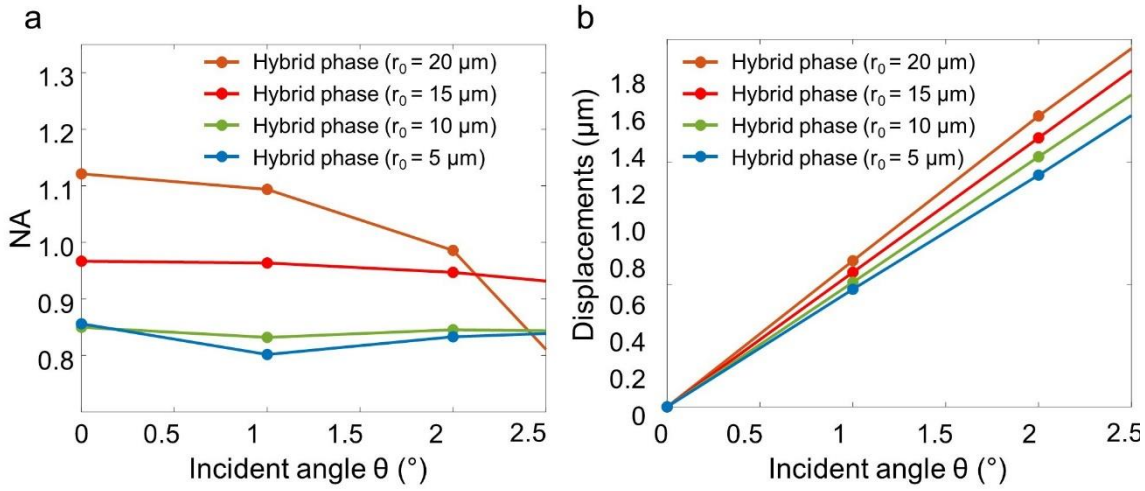

Supplementary Figure 4. Focal spot properties for different boundaries. a NA and SR can be controlled by adjusting r_0. As r_0 increases, the hybrid phase profile resembles the hyperbolic phase profile, and in the opposite case, it becomes the quadratic phase profile. **b** Displacement of the focal spot depends on the boundaries.

Supplementary Note 5: Space-bandwidth product

The space-bandwidth product (SBP) is the number of samples required to precisely recover a bandlimited function in the Whittaker-Shannon sampling theorem. The SBP of an optical system is directly related to its ability to accurately handle inputs and outputs. In a digital holography system, the spatial bandwidth is determined by the number of pixels of the instrument, such as a spatial light modulator or a camera. In the case of an imaging system, SBP is the maximum number of resolvable spots in the field of view (FOV). Here, we calculated the SBP of the metalens to optimize the performance in a FOV of 3 μm, which can cover the size of a bacterium, a representative biological specimen. Supplementary Figure 5a shows resolvable focal spots of the metalens using hyperbolic and quadratic phases. In the case of the hyperbolic phase, there are many resolvable focal spots in the central region; however, the number abruptly decreases in the edge because of the off-axis aberration. Meanwhile, the metalens using the quadratic phase exhibited uniform focal spots. We calculated the SBP by counting the number of spots in each case. Fragmented parts were added and counted. The SBPs were 98 and 89 for the hyperbolic and hybrid phases, respectively. We also obtained the SBP of the hybrid phase for the different boundaries. Supplementary Figure 5b shows resolvable focal spots of the metalens using the hybrid phases. The SBPs were 117, 138, and 133 for boundaries = 16, 18, and

20 μm, respectively. Therefore, we conclude that the hybrid phase with a boundary of 18 μm shows the best performance in an FOV of 3 μm.

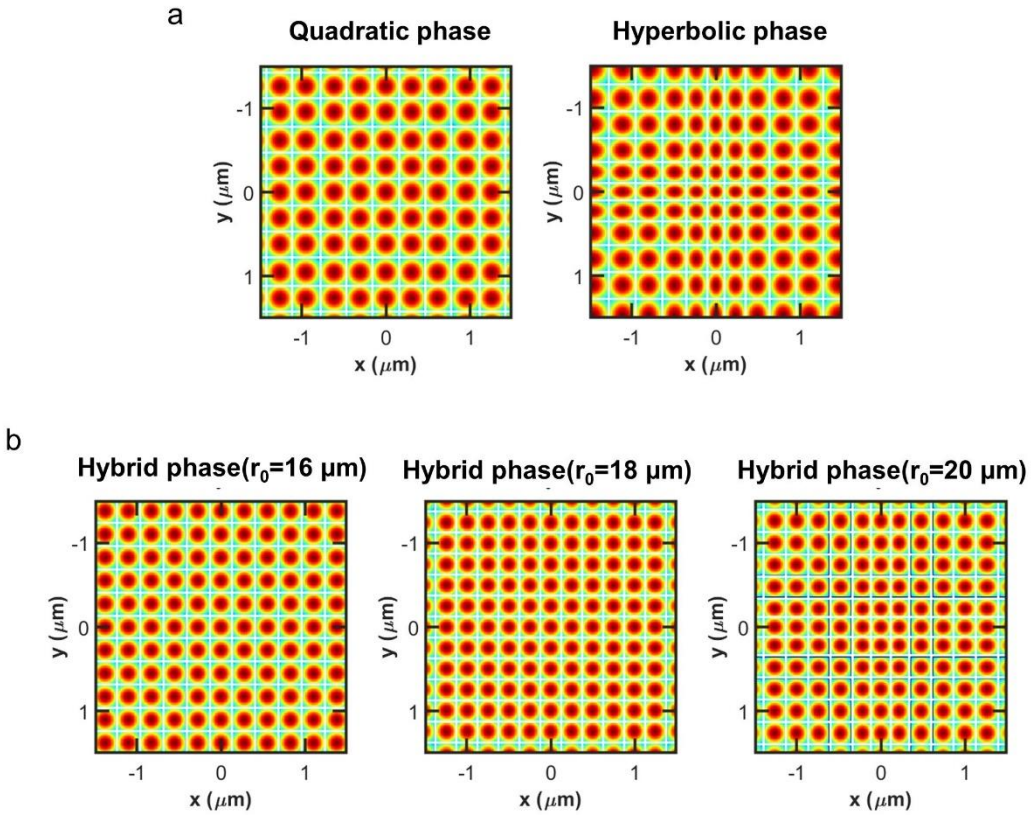

Supplementary Figure 5. a Resolvable focal spots of the metalens using the hyperbolic and quadratic phase. **b** Resolvable focal spots of the metalens using the hybrid phases for the boundary = 16, 18, and 20 μm.

Supplementary Note 6: Finite-difference time-domain simulation results

Because rigorous coupled-wave analysis (RCWA) is a semi-analytical method with a periodic boundary condition, an error can occur for rapid phase modulations corresponding to high-NA metalens. Therefore, we investigated the effect of rapid phase modulation by finite-difference time-domain (FDTD) simulation for a configuration of nanostructures as shown in Supplementary Figure 6a, in which the phase is changed along the x-direction with periodic boundary conditions in the y-direction. As expected, higher-order diffraction occurred for a high NA. However, for an NA lower than 1.0, corresponding to our experiment, the designed diffraction is more dominant than other higher diffractions, as shown in Supplementary Figure 6b and c. Therefore, we can use the nanostructure-phase library calculated by RCWA.

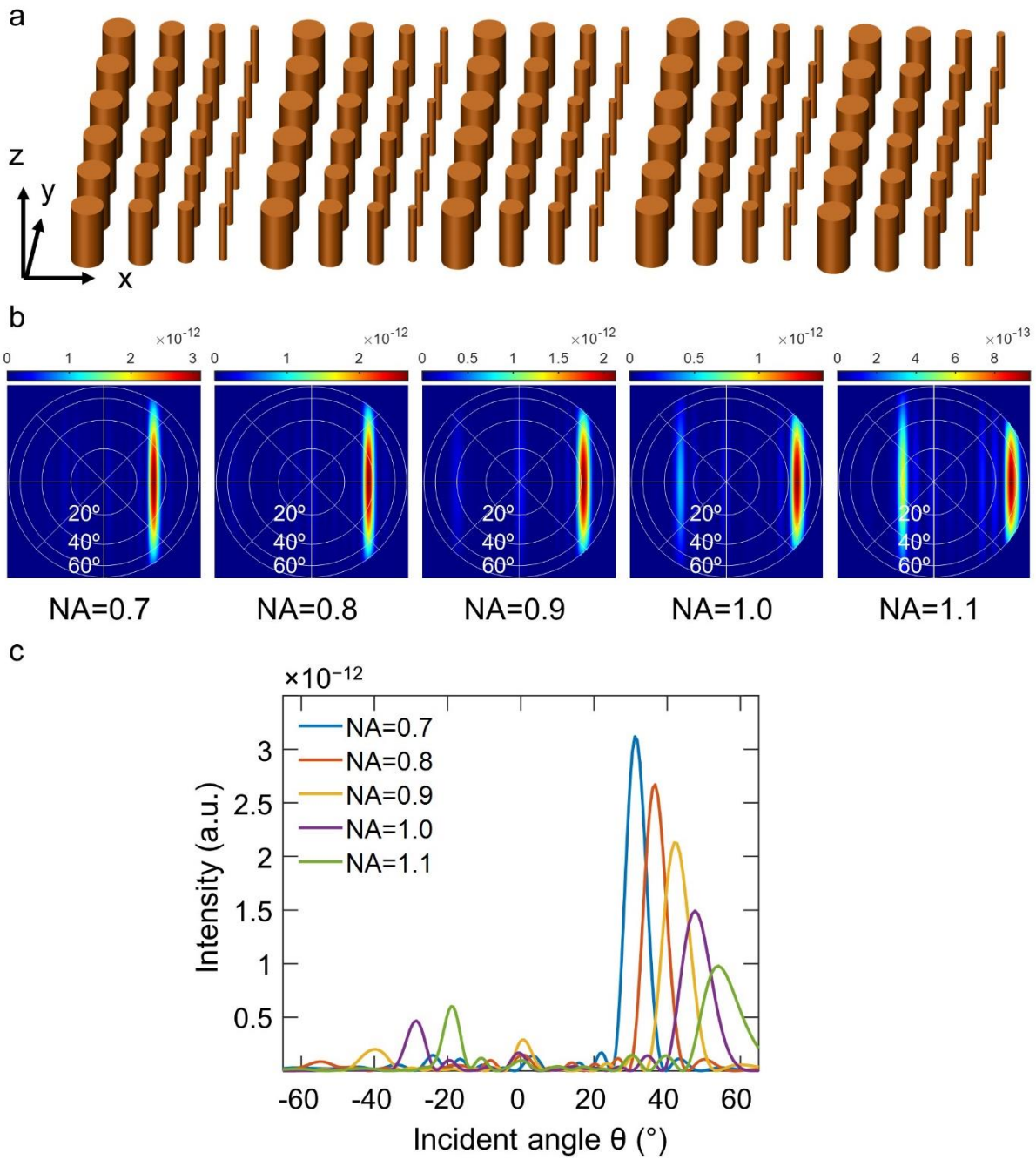

Supplementary Figure 6. a Scheme for FDTD simulation. We consider a configuration of nanostructures, in which the phase is changed along the x-direction with periodic boundary conditions in the y-direction. **b-c** Results of FDTD simulation. As NA increases, higher-order diffractions occur. However, for a lower NA than 1.0, the designed diffraction is more dominant than other higher diffractions.

Supplementary Note 7: Experimental results of the single-focus metalenses using hyperbolic, quadratic phase and hybrid phases.

We fabricated and characterized the single-focus metalens using hyperbolic and quadratic phases. Supplementary Figure 7 shows the measured focal spots. As expected, the measured focal spot of the hyperbolic phase is badly distorted for oblique incidence. In addition, the spot size of the quadratic phase was much larger than that of the hybrid phases. Supplementary Figure 8 shows NAs of these single-focus metalenses for different angles of incidence. Here, we define NA for our metalens as NA= 0.51λ/FWHM, where FWHM is the full width at half maximum of the focal spot. Even though the measured NAs are slightly smaller than the designed NAs, qualitative trends are well matched to the simulations.

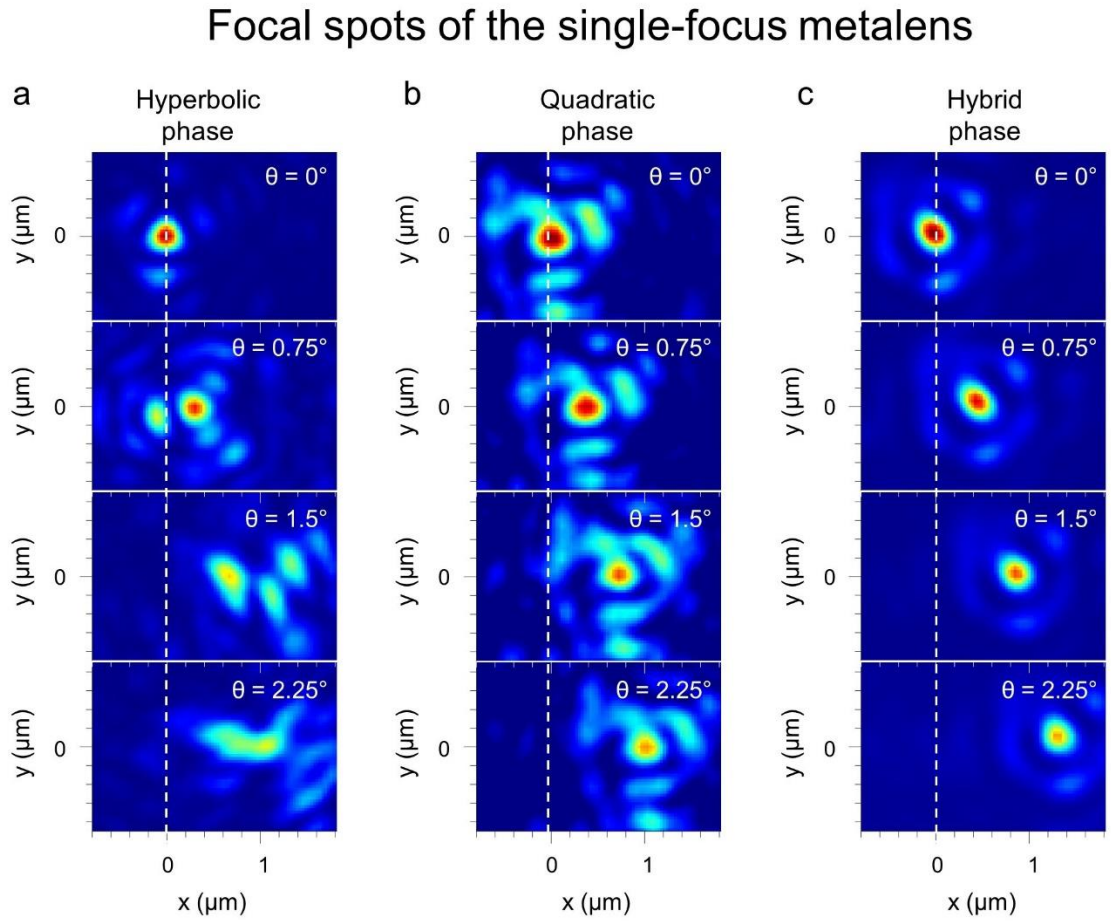

Supplementary Figure 7. Experimentally measured focal spot of the metalens using **a** hyperbolic, **b** quadratic, and **c** hybrid phase profiles.

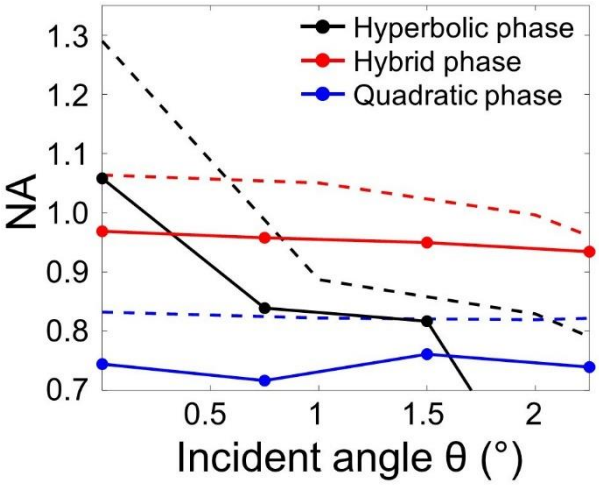

Supplementary Figure 8. NAs of single-focus metalenses for different angles of incidence (Solid line for experiment and dashed line for simulation).

We calculated the focusing efficiency of each case. Here focusing efficiency is defined as the fraction of the incident light that passed through a circular iris in the focal plane with a diameter equal to three times the FWHM of the focal spot. Here, since higher NA than 1.0 is extremely important in the optical tweezers and biological applications, we targeted FWHM as 250 nm, which corresponds to a NA higher than 1.0. Supplementary Figure 9 shows the efficiencies of each phases for different incident angles. We confirmed that the efficiencies of the hybrid phase are larger than others. Note that the advantage of hybrid phase is more apparent for scannable dual-focus metalens. Quadratic phase is not suitable to make dual-focus metalens and hyperbolic phase is not suitable for scanning. Therefore, we think that the hybrid phase is useful for scannable dual-focus metalens.

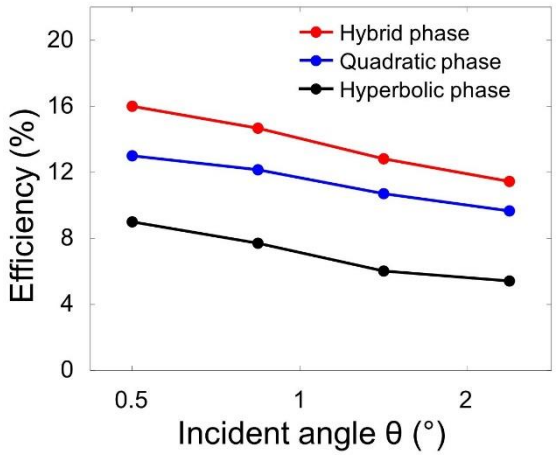

Supplementary Figure 9. Efficiencies of single-focus metalenses using the hybrid, quadratic and hyperbolic phases for different angles of incidence.

Supplementary Note 8: Relationship between the size of metalens and scan range.

We examined the relationship between the size of metalens and scan range. Here, we refer the size of metalens as the diameter with keeping the ratio of the focal length to the diameter (Supplementary Figure 10). The actual value of scanning range depends on the focal length and the scanning range can increase for large metalens. Supplementary Figure 11 shows the FWHM of calculated focal spot for the large metalenses with varying the position of the boundary r_0. The diameters of the metalenses are 320 and 480 μm and the focal lengths are 40 and 60 μm, respectively, corresponding to 2 and 3 times of those of the fabricated metalens in the manuscript. We can select the r_0 = 28 and 36 μm to maximize space-bandwidth product in the FOV of 6 and 9 μm, respectively. These FOVs are corresponding to 2 and 3 times of those of the demonstrated metalens in the manuscript. Supplementary Figure 12 shows the relationship between the size of the metalens and the FWHM of the focal spot using hybrid phase to maximize space bandwidth product. In this paper, we choose the diameter of 160 μm for the smaller FWHM than 250 nm, corresponding to a NA higher than 1.0, because higher NA than 1.0 is extremely important in the optical tweezers and biological applications.

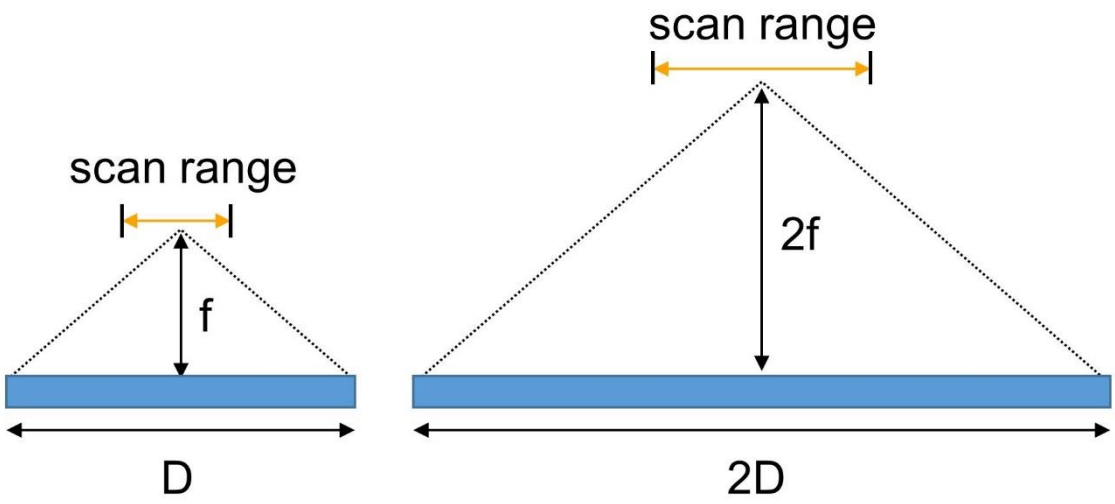

Supplementary Figure 10. The scan range for the large metalens. Since scanning range depends the focal length, scanning range can increase for the large metalens.

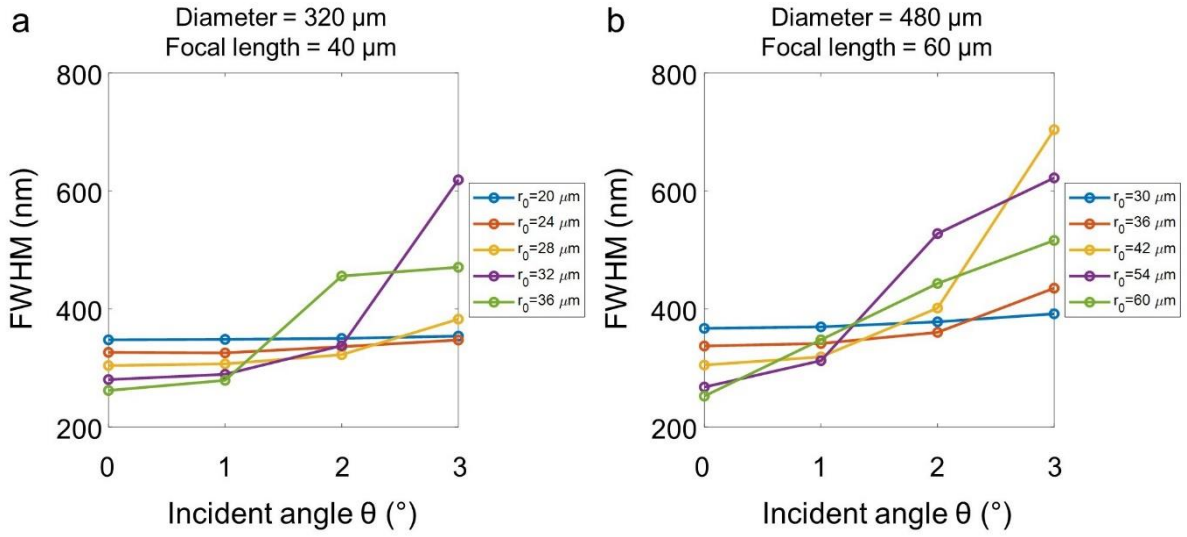

Supplementary Figure 11. The FWHMs of focal spots for the large metalenses with varying the position of the boundary r_0.

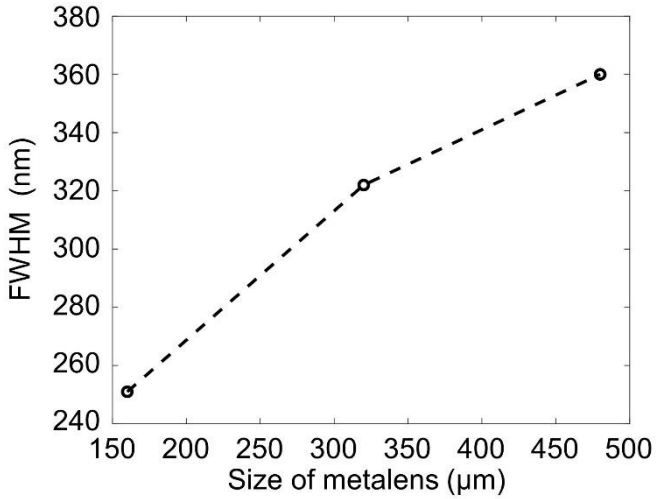

Supplementary Figure 12. The relationship between the size of the metalens and the FWHM of the focal spot using hybrid phase to maximize space-bandwidth product.

Supplementary Note 9: Point spread function broadening of the imaging system

Focal spots were measured by stacking the images at different axial positions. The position of the image plane is adjusted by the position of the oil immersion objective combined with a piezo stage (Figure 4). The mismatch in refractive index between the immersion oil and water results in PSF broadening. Since PSF broadening increases with the focus depth, the focal spot far from the objective is more spread out than the close one. To clarify this point, we calculated the axial intensity distribution of the simulated focal spot with consideration of PSF broadening. Supplementary Figure 13 shows the results with consideration of PSF broadening. When we consider PSF broadening, the intensity profile is much similar to the measured one. Therefore, we conclude that fabrication error and PSF broadening are the reason of the broaden focal spots.

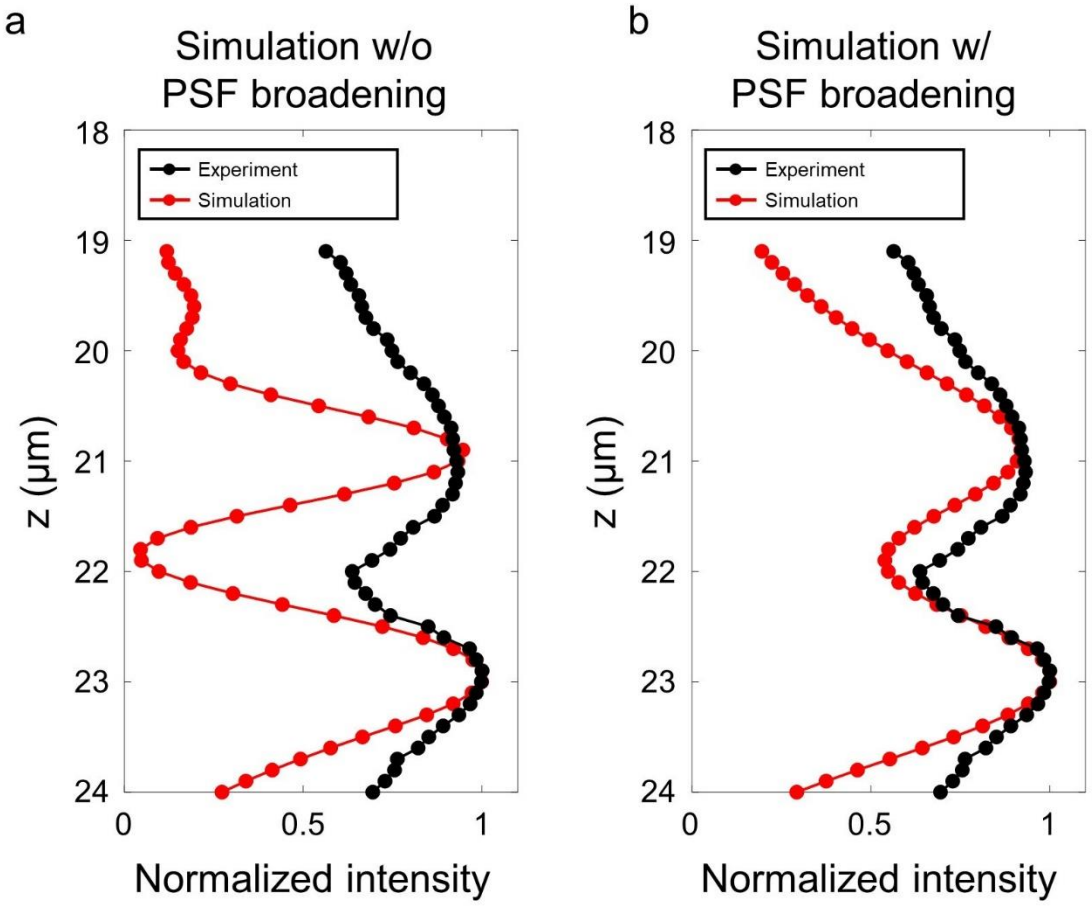

Supplementary Figure 13. The axial intensity profile of the focal spot **a** without consideration of PSF broadening and **b** with consideration of PSF broadening.

Supplementary Note 10: Dual-focus metalens using hyperbolic and quadratic phase

We also examined the dual-focus metalenses with hyperbolic and quadratic phases. In the Gerchberg–Saxton (GS) algorithm, the phase generating two focal spots is assumed to be the superposition of the phases generating individual spots. Therefore, both spots should be well separated to make dual focusing. Specifically, the FWHM along the z-direction should be smaller than 2 μm for dual focusing within 2 μm. Supplementary Figure 14 shows the axial distribution of individual focal spots of hyperbolic, quadratic and hybrid phases for f_1=20 and f_2=22 μm at normal incidence. The horizontal axis of the graph is the relative distance from the peak position f_1. Hyperbolic and hybrid phase meet the condition to make dual focusing within 2 μm. However, the quadratic phase cannot meet the conditions. Therefore, there is no solution to make the dual-focus metalens using quadratic phase. Next, we use the GS algorithm to create a dual-focus phase with hyperbolic phase. The dual-focus phase is characterized from both simulation and experiments. Supplementary Figure 15 shows the calculated and measured focal spots of the dual-focus metalens using hyperbolic phase in a plane containing the optical axis (x-z plane) and two focal planes (x-y planes) for different angles of incidence. Focal spots of the hyperbolic phase are badly distorted for oblique incidence, indicating failure to maintain dual focusing.

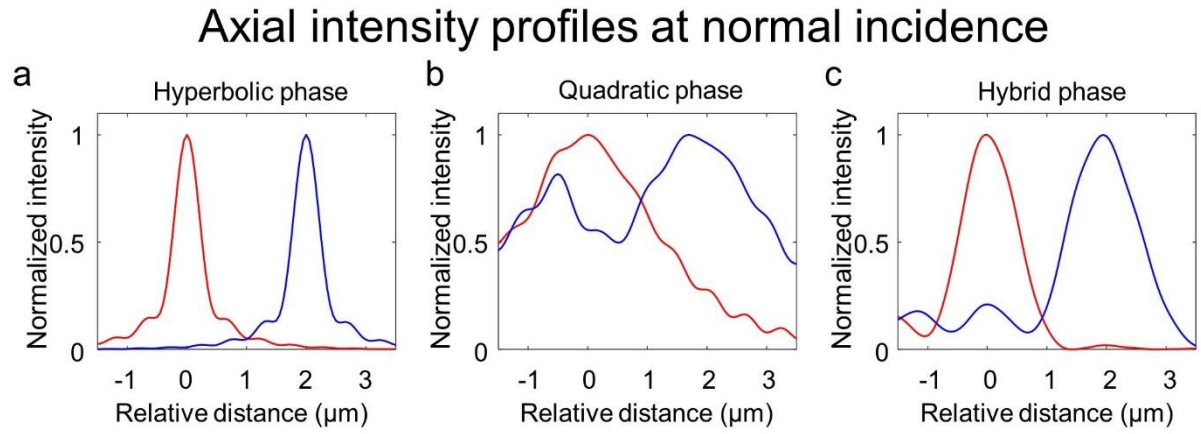

Supplementary Figure 14. The axial intensity profiles of the individual focal spots using for **a** hyperbolic, **b** quadratic and **c** hybrid phases for normal incidence (red lines for f_1 and blue lines for f_2).

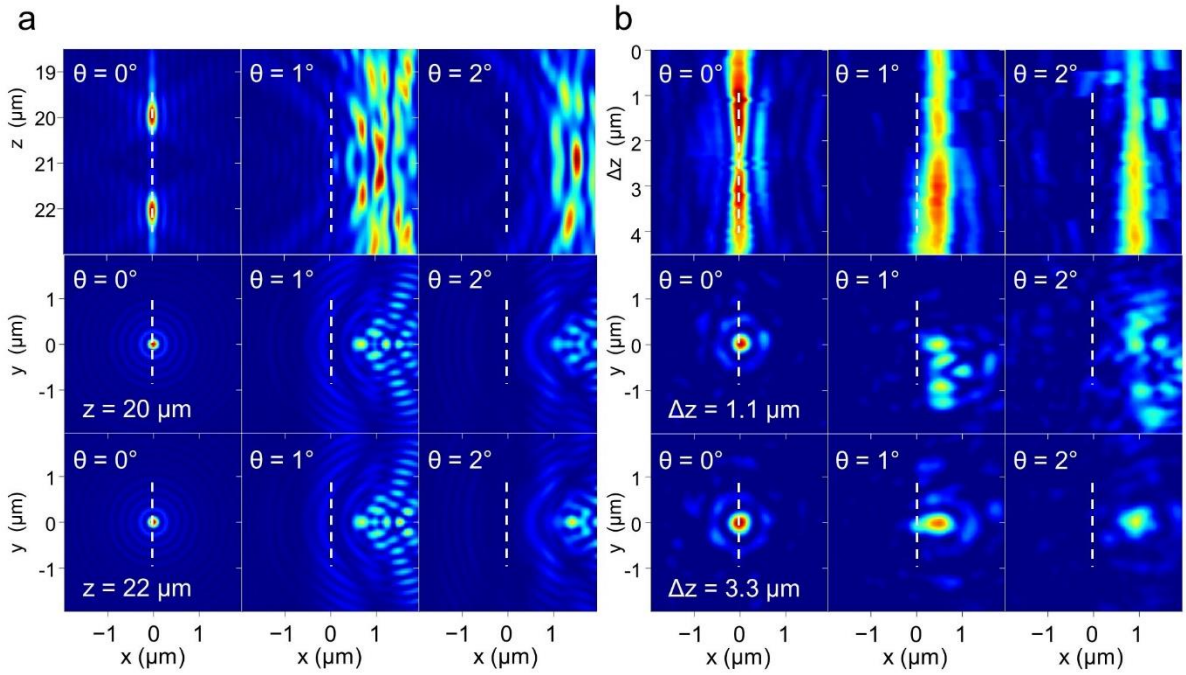

Supplementary Figure 15. a The Calculated and **b** measured focal spots of the dual-focus metalens using the hyperbolic phase in the xz-plane and the focal planes. The positions of the focal plane are Δz = 1.1 μm (corresponding to f_1) and 3.3 μm (corresponding to f_2), where the peak intensity is the local maximum at normal incidence.

Supplementary Note 11: Physical properties of the substrate

Crystalline silicon is used in the visible region, and its high refractive index is particularly advantageous. The small thickness of the meta-atoms partially compensated for the prohibitive absorption coefficient. Owing to its high index and compatibility with large-scale manufacturing technologies, c-Si is suitable for high-NA metalenses. The metalenses were fabricated on 503 nm thick

crystalline silicon on 460 μm thick sapphire as shown in Supplementary Figure 16. Supplementary Figure 17 shows the refractive index and extinction coefficient measured using ellipsometry.

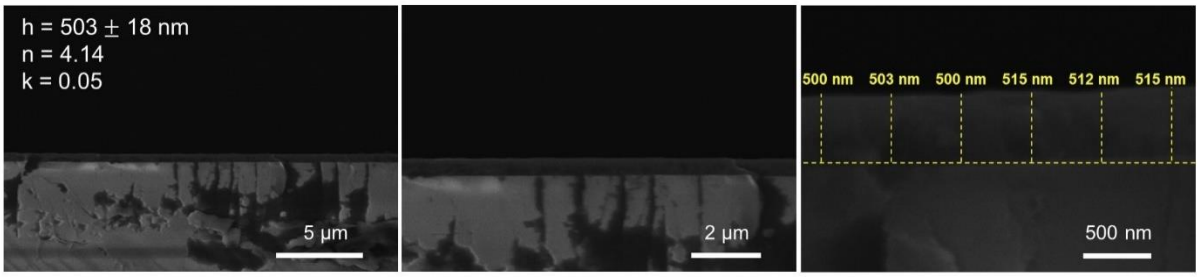

Supplementary Figure 16. Cross-sectional image of a crystalline silicon-on-sapphire taken by SEM. The thickness of c-Si is measured by the cross-section image taken by SEM. The average thickness is 503 nm, and the standard deviation is 18 nm.

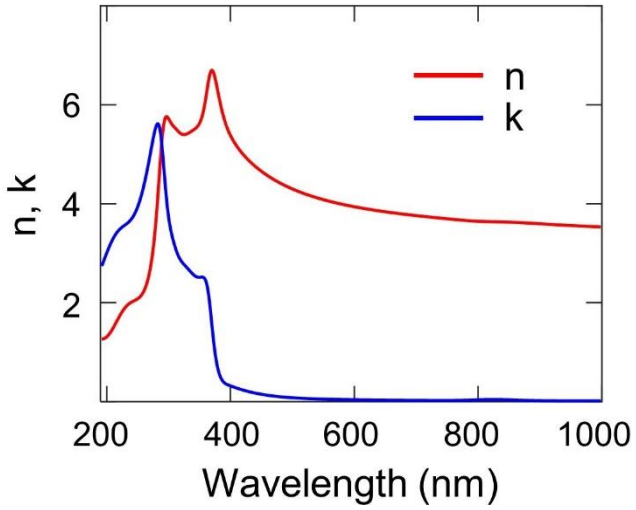

Supplementary Figure 17. Refractive index and extinction coefficient measured by ellipsometry.

Supplementary Note 12: Fabrication process

Supplementary Figure 18 shows the fabrication process of the metalens. The sample was spin-coated with 150 nm PMMA, a positive electron beam resist, and the pattern was generated using electron beam lithography. After development, an electron-beam-evaporated aluminium oxide layer with the thickness of 30 nm was used to reverse the generated pattern using a lift-off process, forming a hard mask. The dry etching was performed using an inductively coupled plasma reactive ion etching process. The aluminium oxide layer was then dissolved in buffered oxide etchant.

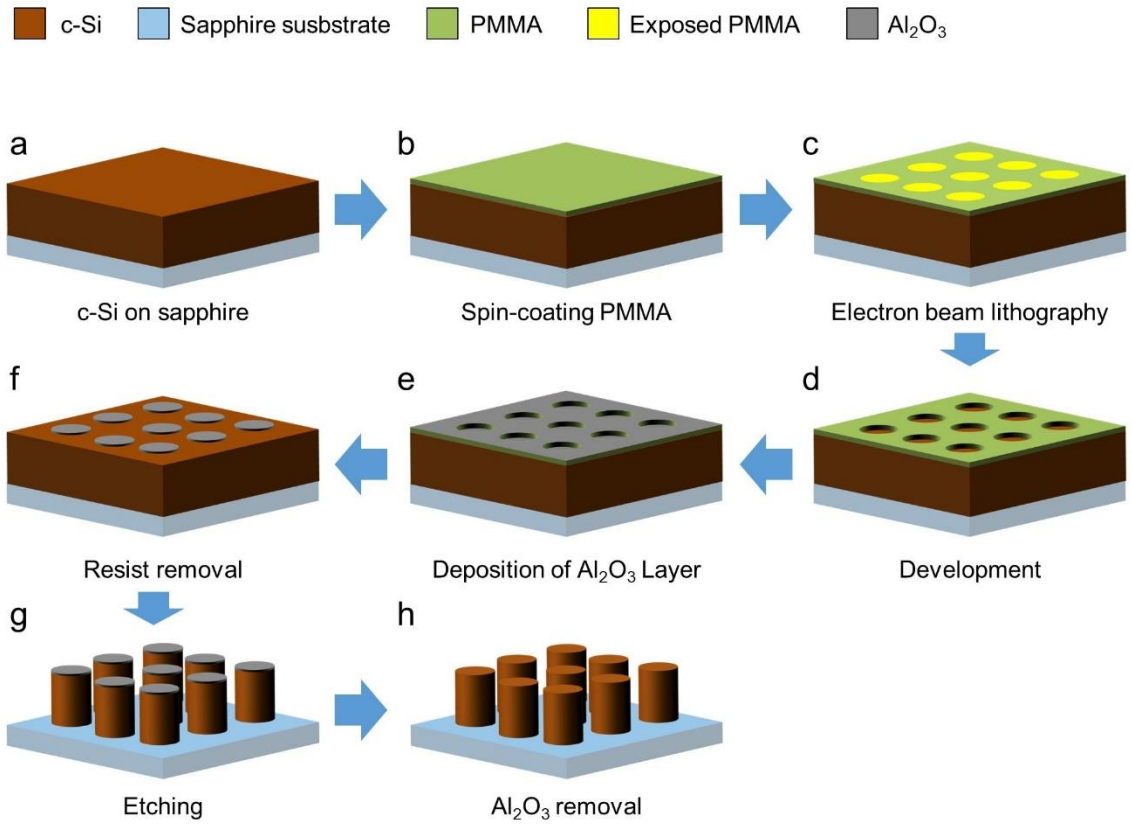

Supplementary Figure 18. Flow for fabrication of a metalens with a hybrid phase profile. a C-Si on the sapphire sample is used to fabricate a metalens with a hybrid phase profile. **b** Positive E-beam resist (PMMA) with the thickness of 150 nm is spin-coated. **c** The pattern was generated using electron beam lithography. **d-f** After development, an electron beam evaporated aluminium oxide layer was used to reverse the generated pattern with a lift-off process, forming the hard mask. **g** The dry etching was performed using an inductively coupled plasma reactive ion etching process. **h** The aluminium oxide layer was then dissolved in BOE etchants.

Supplementary Note 13: Optical setups

Supplementary Figure 19 shows a schematic of the optical setup that characterizes the metalens with a hybrid phase profile. A 532 nm wavelength laser was expanded to a collimated beam with a diameter of 10 mm. The Galvano mirrors control the angle of incidence. The metalenses were located in the sample chamber. After the beam passes through the substrate, the light after the metalens is focused on a spot. The focal spot was measured using a high-NA oil immersion objective lens (Olympus; Plan APO 100×, NA=1.4) mounted on a piezo stage to achieve an image along the z-direction.

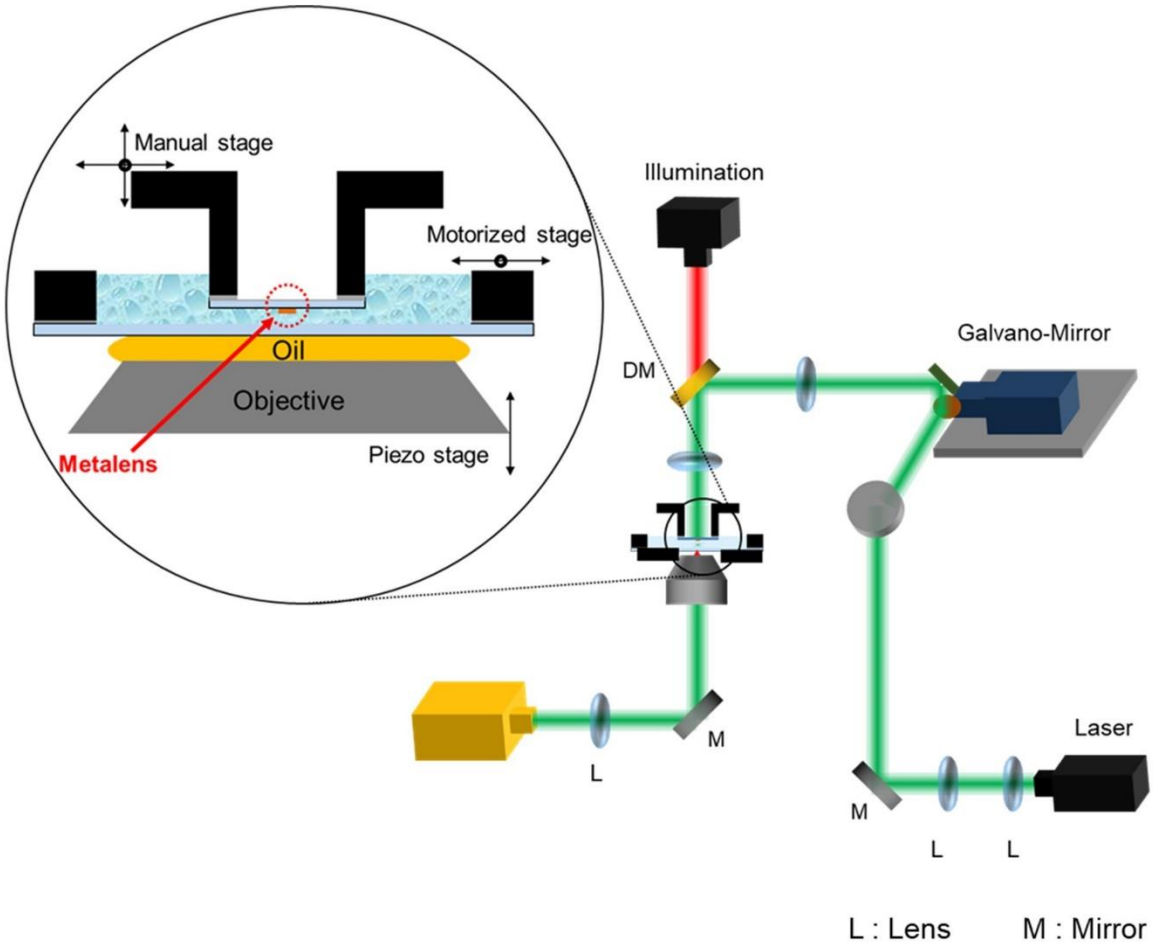

Supplementary Figure 19. Experimental setup to characterize the optical property of the metalens.